Energy Advances

ROYAL SOCIETY OF CHEMISTRY

PAPER

View Article Online
View Journal | View Issue

Cite this: *Energy Adv.*, 2024, 3, 1688

Stabilization of the surface and lattice structure for $LiNi_{0.83}Co_{0.12}Mn_{0.05}O_2$ *via* B_2O_3 atomic layer deposition and post-annealing†

Jiawei Li, Junren Xiang, Ge Yi, Zhijia Hu, Xiao Liu * and Rong Chen *

Received 28th March 2024,
Accepted 20th May 2024

DOI: 10.1039/d4ya00206g

rsc.li/energy-advances

The Ni-rich $LiNi_xCo_yMn_{1-x-y}O_2$ cathode ($x \geq 0.6$) shows weak rate capability due to its deleterious surface lithium impurities and lattice defects. Herein, uniform ultrathin B_2O_3 coatings built by atomic layer deposition (ALD) are utilized to construct a B^{3+} doped single-crystal $LiNi_{0.83}Co_{0.12}Mn_{0.05}O_2$ (SC83) *via* post-annealing. LiOH is consumed due to reacting with B_2O_3 during the B_2O_3 ALD process, and then B_2O_3 is transformed into B^{3+} doping accompanied by the reduction of Li_2CO_3 during the post-annealing. Surface and bulk characterization results show that B^{3+} tends to diffuse into the bulk of the SC83 during the post-annealing, which expands the *a* and *c* axes and reduces the Li^+/Ni^{2+} mixing of the SC83. When the B^{3+} content exceeds 0.54 wt%, B^{3+} segregation occurs on the surface of the SC83, which decreases the electronic conductivity of the SC83. B^{3+} doping at the content of 0.54 wt% gives the highest capacity of 177.6 mA h g^{-1} at 1C rate. The B_2O_3 ALD coupled with post-annealing builds a highly electronic and Li^+ conductive surface and bulk for the SC83, which is the key to the improvement of the rate capability.

Introduction

Lithium-ion batteries with high charge speed are important for shortening the charge time of electric vehicles. The Ni-rich $LiNi_xCo_yMn_{1-x-y}O_2$ cathode (NCM, $x \geq 0.6$), with the advantages of high energy density, low cost, and environmental sustainability, has attracted much attention.[1–3] However, the poor surface and crystal structure of the Ni-rich cathode work against the transfer of Li^+ in the surface and bulk. Resistive surface lithium impurities (LiOH and Li_2CO_3), Li^+/Ni^{2+} mixing, transition metal dissolutions, lattice shrinkage, and intergranular cracking all harm the rate capability of NCM.[4,5] Benefitting from the good mechanical properties, single-crystal NCM shows excellent processability in the manufacture of batteries, which increases its usage in the industry. However, the large grain size of single-crystal NCM decreases its rate capability due to the longer pathways for Li^+ transfer in the bulk.[6,7] Hence, it is extraordinarily significant to enhance the Li^+ diffusivity in single-crystal NCM for achieving the rapid charging of lithium-ion batteries.

Reactive coating is regarded as an effective approach to improve the Li^+ diffusivity in NCM. $Co_3(PO_4)_2$, H_3PO_4, $(NH_4)_2HPO_4$, $H_2C_2O_4$, and Prussian blue have been used to transform surface lithium impurities into highly Li^+ diffusive coatings.[8–13] Although these methods are promising for enhancing Li^+ diffusivity on the surface, they can only give a limited boost to the rate capability of single-crystal NCM, due to the low Li^+ diffusivity in the bulk. Doping is an effective method for optimizing the bulk property of NCM *via* modifying the crystal structure.[14] Various dopants, such as Na^+, F^-, Ce^{3+}, Zn^{2+}, and Mg^{2+}, have been incorporated into the lattice of NCM.[15–20] These dopants effectively improve the rate capability of NCM by enhancing the diffusivity of Li^+ in the bulk. Simultaneously doping and reducing surface lithium impurities has recently been reported by coating and post-annealing as a promising method. Co^{3+}, Al^{3+}, Fe^{3+}, and Ti^{4+} doped NCM are achieved *via* coating combined with post-annealing.[21–23] The surface lithium impurities of all the doped cathodes are reduced, while their rate capabilities also declined. This is attributed to these large ions hardly diffusing into the bulk. They tend to segregate on the surface, which blocks the transfer of electrons and Li^+. As an acidic oxide, B_2O_3 can react with alkaline surface lithium impurities. Moreover, with the advantages of small size but strong B–O bonds, B^{3+} is more likely to diffuse into the NCM from the surface and stabilize the lattice. B^{3+} doped NCM prepared by B_2O_3 coating and post-annealing have recently been reported.[24–27] Although B^{3+} can diffuse into the bulk of NCM, B^{3+} segregation on the surface also occurs.[28,29] B^{3+} segregation reduced the electronic conductivity of NCM, which

State Key Laboratory of Intelligent Manufacturing Equipment and Technology, School of Mechanical Science and Engineering, Huazhong University of Science and Technology, Wuhan 430074, Hubei, People's Republic of China.
E-mail: rongchen@mail.hust.edu.cn, xiaoliu@hust.edu.cn

† Electronic supplementary information (ESI) available. See DOI: https://doi.org/10.1039/d4ya00206g

is against the rate capability of NCM.[29,30] Moreover, B^{3+} segregation induces the surface phase transformation of NCM from layered to rock-salt-like, which is detrimental to the Li^+ transfer on the surface.[31] Atomic layer deposition (ALD), with the virtue of sufficient gas–solid contacts and self-limiting reactions, can produce uniform ultrathin coatings with precise thickness control.[32–36] It is a potential method to investigate the origin of B^{3+} segregation on the surface of NCM.

Here, we investigate the effect of reactive B_2O_3 coatings and B^{3+} doping content on the SC83 *via* B_2O_3 ALD coupled with post-annealing. The ALD growth characterization shows that B_2O_3 grows faster on the surface of LiOH. The surface characterization indicates that the surface LiOH reacts with B_2O_3 and forms $LiBO_x$ during the B_2O_3 ALD process. By performing the post-annealing treatment, the surface Li_2CO_3 is reduced, and B^{3+} diffuses into the bulk of the SC83. Moreover, the *a* and *c* axes of the SC83 expand, and the Li^+/Ni^{2+} mixing of the SC83 decreases, which is influenced by the content of the B^{3+} bulk doping. B^{3+} surface segregation occurs after it saturates in the bulk of the SC83. The saturated B^{3+} bulk doping with virtually no B^{3+} surface segregation gives the highest improvement in the rate capability of the SC83, which results in enhanced electronic conductivity and Li^+ diffusivity of the SC83.

Experimental section

Material preparation

The SC83 was synthesized by a high-temperature calcination method. $LiOH{\cdot}H_2O$ (Shanghai Aladdin Biochemical Technology Co., Ltd) and $Ni_{0.83}Co_{0.12}Mn_{0.05}(OH)_2$ (Ningbo Gaosi New Energy Technology Co., Ltd) powders with the molar ratio of 1.04 : 1 were mixed using a ball-milling method. Subsequently, the mixture was pre-heated at 500 °C for 5 h, then calcined at 850 °C for 12 h under an oxygen atmosphere. Finally, the calcination products are milled into powders to obtain the SC83 materials.

B_2O_3 coatings were coated on the SC83 particles using a homemade rotary ALD reactor. B_2O_3 ALD was performed at 120 °C using trimethyl borate (TMB, Shanghai Aladdin Biochemical Technology Co., Ltd) and H_2O as precursors. In a typical B_2O_3 ALD cycle, 10 s TMB pulse, 60 s exposure time, 60 s N_2 purge, 3 s H_2O pulse, 60 s exposure time, and 60 s N_2 purge are alternately operated. The SC83 particles were coated with B_2O_3 in various ALD cycles. For instance, 0, 2, 6, and 12 ALD cycles of B_2O_3 on the SC83 particles were marked as bare, 2B, 6B, and 12B SC83 particles. After the B_2O_3 ALD process, post-annealing was performed at 500 °C in an oxygen atmosphere for 3 h; the particles were marked as 2B-A, 6B-A, and 12B-A SC83 particles.

Material characterization

The concentration of B was measured *via* an Avio 220 Max (PerkinElmer) inductively coupled plasma-optical emission spectrometer (ICP-OES). The mass uptake during the B_2O_3 ALD process was measured by an SQM-160 (Inficon) quartz crystal microbalance (QCM). For QCM measurement, SC83 particles or Al_2O_3 are loaded on the QCM sensors. The by-products during the B_2O_3 ALD process were monitored by a Dycor LC-D200 (AMETEK) quadruple mass spectrometer (QMS). For QCM and QMS measurements, 1 s TMB pulse, 30 s N_2 purge, 1 s H_2O pulse, and 30 s N_2 purge are alternately operated. The crystalline structure of SC83 was characterized by an X-ray diffractometer (PANalytical X'Pert) with a Cu Ka radiation source. The morphology of SC83 was characterized using a Quanta650 FEG (FEI instrument) scanning electron microscope (SEM) and a Tecnai G2 F20 (FEI instrument) transmission electron microscope (TEM). The surface compositions were detected by an AXIS-ULTRA (Shimadzu-Kratos Co.) X-ray photoelectron spectrometer (XPS). All XPS spectra were aligned by calibrating the C 1s peak at 285 eV. For pH measurements, 5 g of SC83 particles were evenly mixed with 25 ml of deionized water in a beaker to make a slurry. A S210-K pH meter (METTLER TOLEDO) was used to measure the pH of the slurry. For electronic conductivity measurements, SC83 particles were pressed into a mold under a pressure of 20 MPa, then measurements were conducted *via* a multimeter.

Electrochemical measurements

The SC83 cathode slurry was prepared using a *N*-methyl pyrrolidine (NMP) based slurry containing 80 wt% SC83, 10 wt% carbon black, and 10 wt% polyvinylidene fluoride (PVDF). The SC83 cathode slurry was cast on carbon-coated Al foils, then dried in a vacuum oven at 120 °C overnight. The loading of SC83 was approximately 3 mg cm^{-2}. The electrolyte was 1 M $LiPF_6$ in the solvent containing ethylene carbonate (EC), dimethyl carbonate (DMC), and ethyl methyl carbonate (EMC) with a volume ratio of 1 : 1 : 1. Microporous polypropylene membranes (Celgard 2400) were used as the separator. Li foils were used as the anode. The coin cells (CR2025) were assembled in an argon-filled glovebox (MB-Unilab). A Land CT3002A battery tester was used to perform the charge–discharge tests with a voltage range from 3.0 to 4.5 V at the desired current density (1C corresponds to 200 mA g^{-1}) in the temperature of 21 °C. The galvanostatic intermittent titration technique (GITT) measurements were carried out on a Land CT3002A battery tester. The coin cells were firstly given a galvanostatic current of 0.1C in 20 minutes, then followed by a relaxation time of 60 minutes. Electrochemical impedance spectra (EIS) were obtained *via* an Autolab PGSTAT302N electrochemical workstation (Metrohm) over the frequency range from 0.01 Hz to 100 kHz with an amplitude perturbation of ±5 mV.

Results and discussion

Fig. 1a illustrates the B_2O_3 ALD process on the SC83 particles. The details are described and analyzed in the following text. ICP-OES is used to measure the B concentration in the B_2O_3-coated SC83. As shown in Fig. 1b, the B concentrations are linear with the ALD cycles in the first 6 ALD cycles. After 6 ALD cycles, the growth rate of B_2O_3 gradually decreases. The B_2O_3

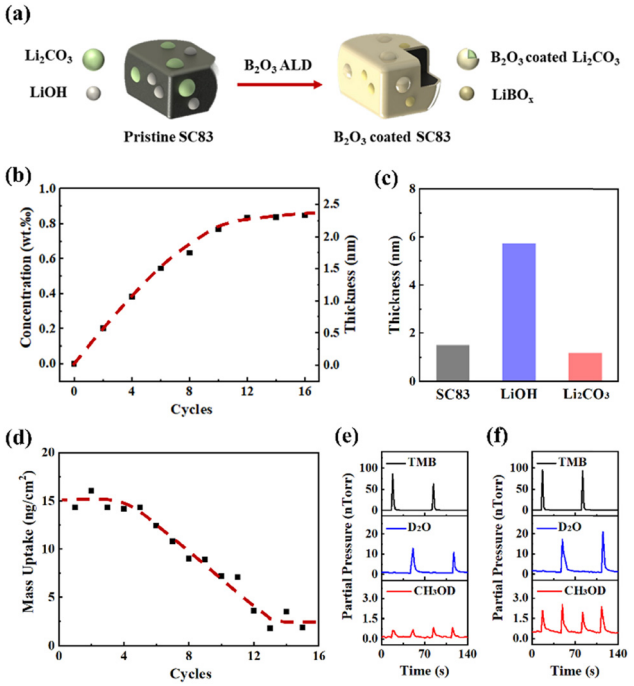

Fig. 1 (a) Schematic illustration of the B_2O_3 ALD on the SC83 particles. (b) B concentration and corresponding calculated B_2O_3 film thickness of the B_2O_3 coated SC83 particles *versus* ALD cycles. (c) Calculated B_2O_3 coating thicknesses of the 6 ALD B_2O_3 coated SC83, LiOH, and Li_2CO_3 particles. (d) Mass uptake from each B_2O_3 ALD cycle on the SC83 particles. Residual gas detection during the B_2O_3 ALD on the (e) SC83 and (f) LiOH particles.

slowly and steadily grows after 12 ALD cycles. Although ALD is regarded as a linear growth process in thin film deposition, actually, the surface compositions of the substrate influence the ALD growth rates in the initial stage.[37,38] Surface LiOH and Li_2CO_3 could induce the variation of the B_2O_3 growth rates on the SC83 particles. Fig. 1c shows the calculated thicknesses of B_2O_3 coatings on the SC83, LiOH, and Li_2CO_3 particles with 6 ALD cycles (the calculation method and relative parameters are shown in the ESI†). The calculated thickness of the B_2O_3 coatings on the LiOH particles is much higher than the theoretical thickness of 6 B_2O_3 molecules (approximately 1.2 nm), suggesting subsurface reactions during the B_2O_3 ALD on LiOH particles. In order to further verify the ALD growth behavior of B_2O_3 on the SC83 particles, *in situ* QCM is used to detect the mass change during the B_2O_3 growth on the SC83 particles. Fig. S1 (ESI†) shows the mass uptake during the B_2O_3 ALD on the SC83 particles. The mass increases in a stair-like shape after each ALD cycle. Fig. 1d shows the mass uptake in each B_2O_3 ALD cycle from Fig. S1 (ESI†). It shows that the mass uptake is constant in the initial stage, and then gradually decreases after the 6th ALD cycle. The mass uptake is low and constant after 12 ALD cycles, indicating a low growth rate of B_2O_3 ALD. These results are consistent with the above ICP-OES results. TMB is easy to chemisorb on the basic surfaces, while it is hard to chemisorb on acidic surfaces, which leads to a gradually decreased growth rate of the B_2O_3 ALD.[34] Fig. S2 (ESI†) shows that the mass uptake from each B_2O_3 ALD cycle on Al_2O_3 gradually decreases to a low and constant value, which further indicates the growth behavior of the B_2O_3 ALD. The difference is that the mass uptake of B_2O_3 ALD on the SC83 particles exhibits a plateau in the initial stage, which may be attributed to the higher surface basicity of SC83 delaying the growth inhibition of the B_2O_3 ALD. For evaluating the reaction intensity of the B_2O_3 ALD on the SC83 and LiOH particles, *in situ* QMS is used to monitor the concentration of the reactants and byproducts during the B_2O_3 ALD process. As shown in Fig. 1e, the black and blue peaks indicate the pulse of TMB and D_2O during the B_2O_3 ALD on the SC83 particles. It is found that the peaks of CH_3OD occur during the TMB and D_2O pulse, which come from the byproducts of the B_2O_3 ALD reactions. A similar phenomenon is found during the B_2O_3 ALD on the LiOH particles, as shown in Fig. 1f. The peaks of CH_3OD for B_2O_3 ALD on the LiOH particles are stronger than that on the SC83 particles, which indicates that the reaction intensity of the B_2O_3 ALD on the LiOH particles is more violent than that on the SC83 particles.

The morphology of the bare, 6B, and 6B-A SC83 particles is observed using SEM. As depicted in Fig. S3 (ESI†), the SC83 particles show polygonal shapes ranging from 2 to 3 μm, and their morphology remains after the B_2O_3 ALD and post-annealing treatment. To examine the B_2O_3 coatings, TEM is performed to characterize the surface morphology of the 6B and 6B-A SC83 particles. As shown in Fig. 2a, the edges of the 6B SC83 particles are smooth. The surface morphology of the 6B SC83 particles is shown in Fig. 2b using high-resolution TEM (HR-TEM). The measured lattice spacing is 0.477 nm, which is assigned to the (003) plane of the SC83.[39,40] The amorphous B_2O_3 coatings with the thickness of 1.4 nm are observed on the surface of the SC83 particles, which agrees with the calculated thickness derived from the ICP-OES results. B is detected at the surface of the 6B SC83 particles, while the atomic concentration of B in the bulk of the 6B SC83 particles is much lower, which further validates the existence of B_2O_3

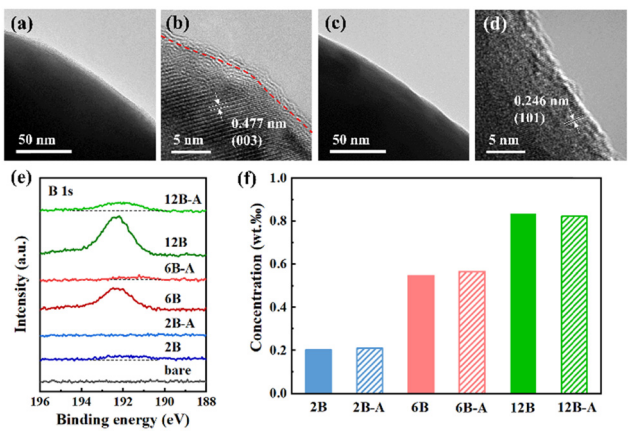

Fig. 2 (a) TEM and (b) HR-TEM of the 6B SC83 particles. (c) TEM and (d) HR-TEM images of the 6B-A SC83 particles. (e) B 1s XPS spectra of the bare, B_2O_3 ALD coated, B_2O_3 ALD coated and annealed SC83 particles. (f) Concentration of B in the B_2O_3 ALD coated, B_2O_3 ALD coated and annealed SC83 particles from ICP-OES results.

coatings (Fig. S4a, ESI†). Besides, amorphous B_2O_3 coatings with the thickness of 2.3 nm are observed on the 12B SC83 particles (Fig. S5, ESI†). As shown in Fig. 2c, the edges of the 6B-A SC83 particles are smooth. The surface morphology of the 6B-A SC83 particles is shown in Fig. 2d. The measured lattice spacing is 0.246 nm, which is assigned to the (101) plane of SC83. No coating is observed on the surface of the 6B-A SC83 particles. Besides, the EDS analysis (Fig. S4b, ESI†) also shows that the atomic concentration of B on the surface of the 6B-A SC83 particles is much lower than that of the 6B SC83 particles. The decreased atomic concentration of B could be attributed to B^{3+} diffusing into the bulk of the SC83 particles after post-annealing. XPS characterization has been performed to investigate the surface composition of the SC83 particles after B_2O_3 ALD and post-annealing. As shown in Fig. 2e, for 2B SC83 particles, a small and broad B 1s peak occurs around 192.0 eV. It is lower than the B 1s peak of B_2O_3 at 192.6–193.0 eV,[41–43] but higher than the B 1s peak of $LiBO_x$ at 190.9–191.8 eV,[44–46] which indicates that B_2O_3 and $LiBO_x$ coexist on the surface of the 2B SC83 particles. The formation of $LiBO_x$ is attributed to B_2O_3 ALD on the surface LiOH. Fig. S6 (ESI†) shows that the B 1s peak occurs at 191.5 eV and 192.7 eV for B_2O_3 coated LiOH and Li_2CO_3, respectively. This indicates that $LiBO_x$ and B_2O_3 formed on LiOH and Li_2CO_3, respectively. As the number of ALD cycles increases, the B 1s peak strengthens, indicating the accumulation of B on the surface. Moreover, the B 1s peak gradually becomes sharp and shifts to a higher position, which indicates that the ratio of B_2O_3 increases in the B_2O_3/$LiBO_x$ hybrid coatings. In the first 2 ALD cycles, much $LiBO_x$ forms due to the subsurface reactions between the B_2O_3 and the LiOH. After the LiOH is gradually consumed, no $LiBO_x$ forms in the subsequent ALD cycles, while the B_2O_3 continuously accumulates. After post-annealing, the B 1s peak decreases, indicating the reduction of the B content on the surface. To investigate the whereabouts of the surface B, ICP-OES was conducted to measure the B content in the SC83 particles. As shown in Fig. 2f, the ICP-OES results show the B content in the SC83 particles before and after post-annealing is almost the same. Combined with the XPS results, this indicates that surface B^{3+} diffuses into the bulk of SC83 particles during the post-annealing. For 2B-A SC83 particles, no B 1s peak is observed, which indicates that all the surface B^{3+} diffuses into the bulk. However, as the content of the B_2O_3 coatings increases, B^{3+} segregation occurs. For 6B-A SC83 particles, only a very small and broad B 1s peak is observed. Moreover, the B 1s peak occurs at the lower position, which indicates that the B_2O_3 coatings are transformed into B^{3+} doping. For 12B-A SC83 particles, the B 1s peak strengthens, which indicates that the B^{3+} segregation escalates. XPS characterization also demonstrates that the O–C═O peak intensity of the SC83 particles noteworthily declines after B_2O_3 ALD and post-annealing, reflecting that the content of the surface Li_2CO_3 decreases[47,48] (Fig. S7, ESI†). The decreased pH of the SC83 slurry after B_2O_3 ALD and post-annealing further validates the reduction of surface lithium impurities (Fig. S8, ESI†).

The crystal structures of bare, 6B, and 6B-A SC83 particles are analyzed *via* XRD. As shown in Fig. 3a, all samples show well-separated (006)/(012) peaks and (108)/(110) peaks, implying a typical α-$NaFeO_2$ layered structure. No extra peaks and no peak shifts are detected in the XRD patterns of the 6B SC83 particles, indicating that the B_2O_3 ALD process does not change the crystal structure of the SC83. As shown in Fig. 3b, the (003) peak of the 6B-A SC83 particles shifts to the lower position, which reflects the increase of the (003) interplanar spacing. The (003)/(104) ratios of the bare, 6B and 6B-A SC83 particles are 1.37, 1.35 and 1.87, respectively. The B_2O_3 ALD process barely changes the (003)/(104) ratios, but combined with the post-annealing, the (003)/(104) ratios increase much, which reflects the decrease of the Li^+/Ni^{2+} mixing. The lattice parameters of the bare, B_2O_3 ALD coated, annealed, and B_2O_3 ALD coated coupled with annealed SC83 are calculated from the XRD patterns using Rietveld refinement (Fig. S9 and Table S2, ESI†). As shown in Fig. 3c, the *a* and *c* axis lengths of the bare, 2B, 6B, 12B, bare-A SC83 are almost the same, which indicates that B_2O_3 ALD or annealing barely influences the lattice of the SC83. For B^{3+} doped SC83, the *a* and *c* axes expand, which is attributed to the B^{3+} being likely to occupy the tetrahedral gaps of the packed oxygen in the Li and TM layers, thus expanding the lattice parameters of the SC83.[49,50] Moreover, B^{3+} doping decreases the Li^+/Ni^{2+} mixing of SC83 initially (shown in Fig. 3d), which could be attributed to the B^{3+} blocking the

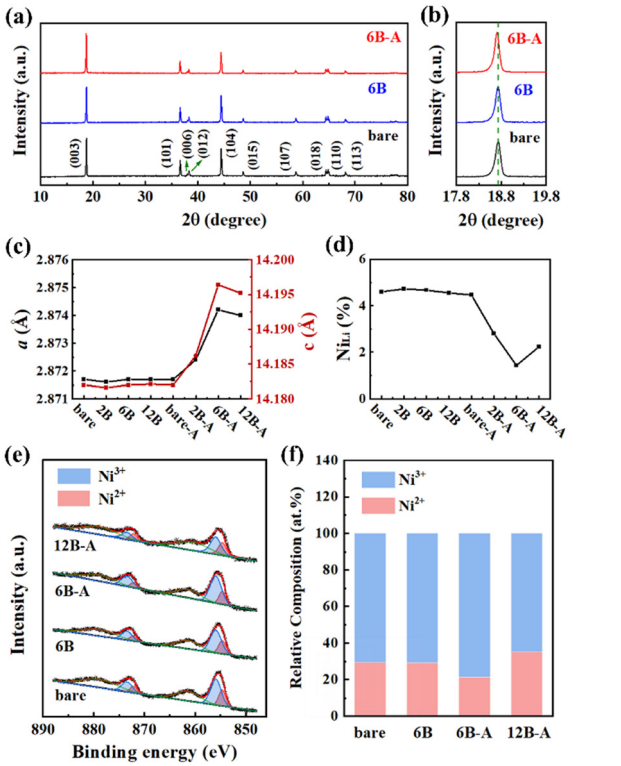

Fig. 3 (a) XRD patterns and (b) magnified regions of the (003) peak for the bare, 6B, and 6B-A SC83 particles. (c) *a* and *c* axis lengths of the bare, B_2O_3 ALD coated, annealed, and B_2O_3 ALD coated coupled with annealed SC83 samples. (d) Li^+/Ni^{2+} mixing degree of the bare, B_2O_3 ALD coated, annealed, and B_2O_3 ALD coated coupled with annealed SC83 samples. (e) XPS spectra of Ni 2p and (f) relative composition of the Ni valence for bare, 6B, 6B-A and 12B-A SC83 particles.

migration pathway of Ni ions to the Li sites through the tetrahedral sites in the Li layers.[51] However, as the content of B^{3+} doping further increases, the expansion of the *a* and *c* axes and the reduction of the Li^+/Ni^{2+} mixing slightly declines for 12B-A SC83 due to the excess B^{3+} accelerating Ni^{3+} to Ni^{2+} transformations for charge compensation.[27] Furthermore, XPS analysis is carried out to compare the valence states of surface Ni for the bare, 6B, 6B-A, and 12B-A SC83 particles. As shown in Fig. 3e, two main peaks at 855.5 eV and 873.0 eV can be assigned to Ni $2p_{3/2}$ and Ni $2p_{1/2}$, which can be split into two pairs of binding energies corresponding to Ni^{2+} (854.7 eV and 872.2 eV) and Ni^{3+} (856 eV and 873.5 eV). The relative composition of Ni^{2+} and Ni^{3+} is calculated according to the peak area and shown in Fig. 3f. The B_2O_3 ALD does not change the Ni^{2+} content on the surface. An obvious reduction of Ni^{2+} content occurs after post-annealing, which indicates the reduction of the surface Li^+/Ni^{2+} mixing. However, the surface Ni^{2+} content increases for the 12B-A SC83 particles, which further illustrates that the excess B^{3+} will induce Li^+/Ni^{2+} mixing.

The electrochemical performance of the bare and coated SC83 cathodes was measured. Fig. 4a shows the rate capability of the bare, 6B, and 6B-A SC83 cathodes. As the charge–discharge rate increases, the gaps of the capacity among each cathode become more pronounced, and the 6B-A SC83 cathode gives the highest capacity. Fig. S10a (ESI†) also shows the rate capability of the 2B, 6B, and 12B SC83 cathodes, all of which exhibit lower capacity compared to the bare SC83 cathode. As the B_2O_3 ALD cycles increase, the rate capability of the SC83 cathodes further decays, which could be attributed to the regressive electronic conductivity of the SC83 particles (Fig. S11, ESI†). Besides, the B_2O_3 coatings may also block the transfers of Li^+. After post-annealing, the rate capability of the B_2O_3 coated SC83 cathodes is improved (Fig. S10b, ESI†), which could be attributed to the enhanced electronic conductivity of the SC83 particles (Fig. S11, ESI†). Moreover, B_2O_3 ALD coupled with post-annealing enlarges the *a* and *c* axes and reduces the Li^+/Ni^{2+} mixing of SC83, which is beneficial to the Li^+ diffusivity. The 6B-A SC83 cathode shows the largest *c* axis with the lowest Li^+/Ni^{2+} mixing, which is responsible for the best rate capability. Although the 12B-A SC83 cathode shows similar lattice parameters to the 6B-A SC83 cathode, inferior electronic conductivity may limit its capacity release. Fig. 4b shows the mean discharge voltage of the bare, 6B, and 6B-A SC83 cathodes at 0.1–2C rate. As the charge–discharge rate increases, the mean discharge voltage difference among each cathode increases, and the 6B-A SC83 cathode shows the highest mean discharge voltage, indicating the lowest polarizations. A cycling test is performed to evaluate the electrochemical stability of the SC83 cathodes. As shown in Fig. 4c, the capacity of the bare, 6B, and 6B-A SC83 cathodes starts at 173.5, 171.2 and 177.6 mA h g^{-1} and ends at 71.4, 77.2 and 116.6 mA h g^{-1}, corresponding to the capacity retention of 41.2, 45.1, and 65.7% after 300 charge–discharge cycles. The 6B-A SC83 cathode shows much higher capacity retention than the bare and 6B SC83 cathodes. The cycling stability of the B_2O_3 coated SC83 cathodes with different ALD cycles is similar and almost the same as the bare SC83 cathode (Fig. S10c, ESI†). This may originate from the insufficient reaction of TMB during the B_2O_3 ALD inducing defects in the B_2O_3 coatings, which make it not dense enough to protect the SC83 cathode from the erosion of the electrolyte.[34] After post-annealing, the B_2O_3 coated SC83 cathodes show enhancements in cycling stability (Fig. S10d, ESI†).

The capacity retention of the SC83 cathodes increases as the number of B_2O_3 ALD cycles increases from 2 to 6. The 12B-A SC83 cathode shows similar capacity retention to the 6B-A SC83 cathode, while the 12B-A SC83 cathode gives lower capacity after cycling due to the lower initial capacity. Fig. 4d shows the mean discharge voltage during cycling. The 6B-A SC83 cathode shows the highest mean discharge voltage from the beginning to the end, and exhibits the slowest voltage decay. Fig. S12 (ESI†) shows the discharge curves of bare, 6B, and 6B-A SC83 cathodes during cycling. The 6B-A SC83 cathode exhibits visible plateaus even after 300 charge–discharge cycles. The capacity release ability of the 6B-A SC83 cathodes is great compared with NCM modified by other methods reported in the literature (Table S3, ESI†). Moreover, the repeated rate capability and cycling stability results of the bare and 6B-A SC83 cathodes show that their capacity release ability is stable (Fig. S13, ESI†). The 6B-A SC83 cathode also shows better storage stability at high temperature compared to the bare SC83 cathode (Fig. S14, ESI†). Besides, the rate capability and cycling stability of the bare-A SC83 cathode are almost the same as those of the bare SC83 cathode, which indicates that the performance improvements should be attributed to the transformations of the B_2O_3 coatings into B^{3+} doping during the annealing (Fig. S15, ESI†).

In order to investigate the origin of the enhanced rate capability of the B^{3+} doped SC83 cathodes, GITT tests were performed to measure the Li^+ diffusivity. The GITT curves of the bare and B^{3+} doped SC83 cathodes (Fig. S16, ESI†) indicate that the polarization of the B^{3+} doped SC83 cathodes is lower than that of the bare SC83 cathode, especially when the voltage is

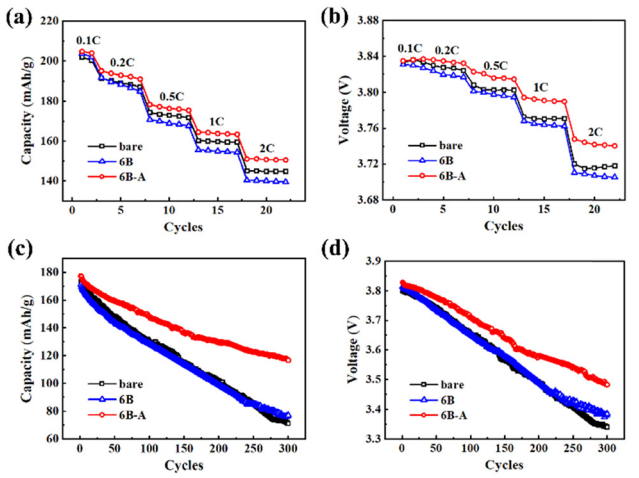

Fig. 4 (a) Rate capability of the bare, 6B and 6B-A SC83 cathodes. (b) Mean discharge voltage of the bare, 6B, and 6B-A SC83 cathodes at 0.1–2C. (c) Cycling stability of the bare, 6B, and 6B-A SC83 cathodes at 1C. (d) Mean discharge voltage of the bare, 6B, and 6B-A SC83 cathodes at 1C.

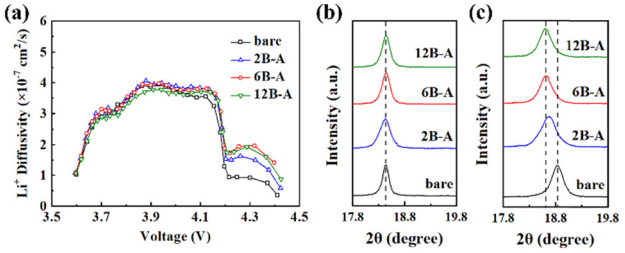

Fig. 5 (a) Li^+ diffusivity of the bare, 2B-A, 6B-A and 12B-A SC83 cathodes during the charge process. The magnified region of the (003) peaks of the bare 2B-A, 6B-A and 12B-A SC83 cathodes at (b) 4.1 V and (c) 4.4 V.

4.2 V. Fig. 5a shows the Li^+ diffusivity of the bare and B^{3+} doped SC83 cathodes during the charge process calculated from the GITT measurements. The 2B-A and 6B-A SC83 cathodes show a little higher Li^+ diffusivity than the bare and 12B-A SC83 cathodes below 4.2 V, which is attributed to the higher electronic conductivity for the 2B-A and 6B-A SC83 cathodes. As the voltage increases, all curves show a sharp decline. This is attributed to the H2–H3 phase transition of SC83 around 4.2 V leading to serious shrinkage of the *c* axis, which reduces the Li^+ diffusivity. It is noteworthy that the Li^+ diffusivity of the B^{3+} doped SC83 cathodes is much higher than that of the bare SC83 cathode upon 4.2 V. The Li^+ diffusivity of the 6B-A and 12B-A SC83 cathodes is similar, while both are higher than that of the 2B-A SC83 cathode. The similar phenomenon is also observed during the discharge process (Fig. S17, ESI†). The highest Li^+ diffusivity of the 6B-A SC83 cathode is responsible for the highest rate capability of it. XRD measurements are performed to measure the *c* axis length of the SC83 cathodes below and upon 4.2 V (Fig. S18, ESI†). As shown in Fig. 5b, all cathodes show the same position of the (003) peak at 4.1 V, which indicates that the *c* axis length among them is the same. As the voltage increases to 4.4 V, the (003) peaks of all the SC83 cathodes shift to higher positions at 4.4 V, while the (003) peak of the B^{3+} doped SC83 cathode shows much fewer shifts than that of the bare SC83 cathode (Fig. 5c). The 6B-A and 12B-A SC83 cathodes show almost the same position of the (003) peaks at 4.4 V, and they show lower position of the (003) peaks than the 2B-A SC83 cathode at 4.4 V. The calculated *c* axis length of the bare and 6B-A SC83 respectively decrease by 0.2808 Å and 0.1152 Å from 4.1 V to 4.4 V, which indicates that 6B-A SC83 exhibits a 59.0% lower shrinkage of the *c* axis compared to the bare SC83 during the H2–H3 phase transition. The long *c* axis is beneficial to the transfer of Li^+, which explains the much higher Li^+ diffusivity of the 6B-A SC83 cathode than the bare SC83 cathode at 4.4 V. According to the above phenomena, it could be inferred that B^{3+} exists in the Li layers. B^{3+} plays the role of the pillar ions to support the Li layers, which alleviates the shrinkage of the *c* axis for SC83 during the H2–H3 phase transition. Hence, it induces better Li^+ kinetics for the SC83 cathode upon 4.2 V. Moreover, the content of B^{3+} bulk doping influences the support to the lattice of the SC83. As the content of B^{3+} doping increases, the support to the lattice increases until B^{3+} is saturated in the bulk of the SC83.

The differential capacity plots are analyzed to understand the electrochemical behavior of the bare and 6B-A SC83 cathodes during the charge–discharge cycling. As shown in Fig. 6a, three redox peaks represent the transition of the bare SC83 cathode from hexagonal to monoclinic phase (H1–M), monoclinic to hexagonal phase (M–H2), and hexagonal to hexagonal phase (H2–H3) at the 4th charge process, respectively. While at the 300th charge process, only one redox peak representing the H1–M phase transition can be distinguished. Moreover, the peak notably shifts to the right, accompanied by a decline in intensity. In contrast, for the 6B-A SC83 cathode, three redox peaks still can be distinguished after cycling (Fig. 6b). Moreover, both the shift of the peak position and the decline of the peak intensity are less, indicating better reversibility. This phenomena can also be observed during the discharge process. It indicates that the 6B-A SC83 cathode suffers from less degradation during the charge–discharge cycling. Fig. 6c shows the EIS of the bare and 6B-A SC83 cathodes after the 4th charge–discharge cycle at the charged state. The surface film impedance (R_f) of the bare and 6B-A SC83 cathodes is similar, while the charge transfer resistance (R_{ct}) of the 6B-A SC83 cathode is lower than the bare SC83 cathode, indicating higher kinetics of Li ions at the interface between the 6B-A SC83 cathode and electrolyte. Moreover, the impedance at low-frequency reflects the Li^+ diffusivity in the bulk of the SC83 cathode. The slope of the 6B-A SC83 cathode is lower than that of the bare SC83 cathode, which indicates faster Li^+ diffusivity in the bulk of the 6B-A SC83 cathode (Fig. S19, ESI†). This is consistent with the GITT results. As shown in Fig. 6d, the R_{ct} of the 6B-A SC83 cathode is much lower than that of the bare SC83 cathode after cycling.

Furthermore, the increase of R_{ct} for the 6B-A SC83 cathode is also much lower than that of the bare SC83 cathode, which demonstrates a more robust interface between the 6B-A SC83 cathode and the electrolyte.

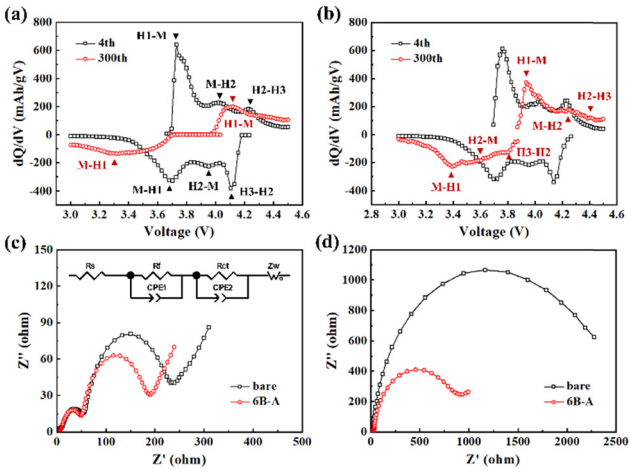

Fig. 6 Differential capacity *versus* voltage profiles of the (a) bare and (b) 6B-A SC83 cathodes at the 4th and 300th charge–discharge cycles. EIS of the bare and 6B-A SC83 cathodes after (c) the 4th charge–discharge cycle and (d) the 300th charge–discharge cycle at the charged state.

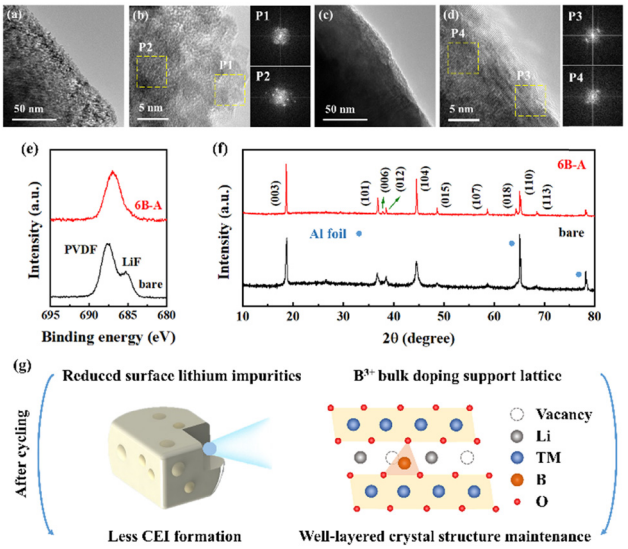

Fig. 7 (a) TEM and (b) HR-TEM of the bare SC83 cathode recovered from the coin cells after cycling. (c) TEM and (d) HR-TEM images of the 6B-A SC83 cathode recovered from the coin cells after cycling. The FFT spectra of the marked locations are shown at the right of the corresponding HR-TEM images. (e) F 1s XPS spectra and (f) XRD patterns of the bare and 6B-A SC83 cathodes recovered from the coin cells after cycling. (g) Schematic illustration of the surface and crystal structure of 6B-A SC83 during cycling.

To investigate the degradation mechanisms of the SC83 cathodes at a microscopic level during cycling, the SC83 cathodes recovered from the coin cells are observed by SEM. As shown in Fig. S20 (ESI†), fewer spotty species are observed on the surface of the 6B-A SC83 cathode than the bare SC83 cathode, suggesting less formation of cathode electrolyte interface (CEI) layers on the surface of the 6B-A SC83 cathode.[52] Furthermore, TEM is performed to characterize the surface morphology of the bare and 6B-A SC83 cathodes. The smooth edges and well single crystalline layered structure are observed on the surface and interior of the bare and 6B-A SC83 cathodes before cycling (shown in Fig. S21, ESI†), while changes happen after cycling. As shown in Fig. 7a, the edges of the bare SC83 particles are rough. Fig. 7b exhibits the rock salt NiO-like and amorphous structure on the surface of the bare SC83. The amorphous structure may be converted from the rock salt NiO-like structure.[53] Besides, polycrystalline domains are observed on the interior of the bare SC83, which may be due to the severe deformation of the layered structure.[53] In contrast, the edges of the 6B-A SC83 are smooth (shown in Fig. 7c). The single crystalline layered structure is observed on the surface and interior of the 6B-A SC83, though the lattice distortion still occurs on the surface of the 6B-A SC83 (shown in Fig. 7d). These results indicate that the surface structure stability of 6B-A SC83 is better than that of bare SC83 during cycling. XPS characterization is performed to detect the F containing species on the surface of the SC83 cathode. As shown in Fig. 7e, the F 1s peaks at 685.1 eV and 687.5 eV can be assigned to LiF and PVDF, respectively.[54] The intensity of the F 1s peak at 685.1 eV for the 6B-A SC83 cathode is much lower than that of the bare SC83 cathode, which indicates much less LiF formation on the surface of the 6B-A SC83 cathode during cycling. As LiF is detrimental due to the sluggish Li^+ transport kinetics, less LiF formation on the surface is beneficial to the capacity retention of the SC83 cathodes. Moreover, XRD characterization is carried out to investigate the crystal structure of the cycled SC83 cathodes. As shown in Fig. 7f, the full width at half-maximum (FWHM) of the peaks for the bare SC83 cathode is much broader than that of the 6B-A cathode, which indicates a lower crystallinity of the bare SC83 cathode after cycling. Moreover, the well-separated (006)/(012) peaks and (108)/(110) peaks can be distinguished in the 6B-A SC83 cathode, while not in the bare SC83 cathode. This indicates that 6B-A SC83 keeps a well-layered crystal structure after cycling, while the bare SC83 does not. The above results show that the B_2O_3 ALD coupled with post-annealing stabilizes the surface and crystal structure of the SC83. As represented in Fig. 7g, the reduced surface lithium impurities decrease the CEI formation on the SC83 during cycling. The B^{3+} bulk doping supports the lattice, which better maintains the crystal structure of the SC83 during cycling. This better preserves the Li^+ transferring channels and storing sites in the B^{3+} doped SC83, hence leading to higher capacity retention for the B^{3+} doped SC83 cathode.

Conclusions

In summary, B^{3+} doped SC83 is constructed by B_2O_3 ALD coupled with post-annealing. Surface LiOH can be consumed and transformed into $LiBO_x$ during the B_2O_3 ALD process, whereas surface Li_2CO_3 can be reduced during the post-annealing treatment. B_2O_3 coatings can be transformed into B^{3+} doping after post-annealing, which expands the *a* and *c* axes and reduces the Li^+/Ni^{2+} mixing of the SC83. B^{3+} is found to diffuse into the bulk of the SC83 during the post-annealing. As B^{3+} is saturated in the bulk, excess B^{3+} is left on the surface of the SC83. Saturated B^{3+} bulk doping with virtually no B^{3+} surface segregation gives the highest improvement in the rate capability of the SC83 cathodes. This is attributed to the reduced surface lithium impurities, decreased Li^+/Ni^{2+} mixing, expanded lattice, and alleviated *c* axis shrinkage during the H2–H3 phase transition, which improves the electronic conductivity and Li^+ diffusivity of the SC83. Besides, the cycling stability of the SC83 cathode is also improved due to the reduced formation of deleterious CEI layers and better crystal structure maintenance. Our study offers ideas for simultaneously stabilizing the surface and crystal structure of NCM.

Author contributions

Jiawei Li: conceptualization, methodology, investigation, formal analysis, writing – original draft. Junren Xiang: methodology and investigation. Ge Yi: visualization. Zhijia Hu: investigation. Xiao Liu: writing – review & editing, supervision. Rong Chen: writing – review & editing, supervision.

Conflicts of interest

There are no conflicts of interest to declare.

Acknowledgements

This work is supported by the National Key Research and Development Program of China (2022YFF1500400), the National Natural Science Foundation of China (51835005, 52350349), and the New Cornerstone Science Foundation through the XPLORER PRIZE. We acknowledge the valuable comments and suggestions from Prof. Bin Shan. We would also like to acknowledge the technology support from the Analytic Testing Center and Flexible Electronics Research Center of HUST.

Notes and references

1 H.-H. Ryu, K.-J. Park, C. S. Yoon and Y.-K. Sun, *Chem. Mater.*, 2018, **30**, 1155–1163.
2 J. Zhang, Y. Jin, J. Liu, Q. Zhang and H. Wang, *Sustainable Energy Fuels*, 2021, **5**, 5114–5138.
3 Y. Huang, *Interdiscip. Mater.*, 2022, **1**, 323–329.
4 J. Kim, H. Lee, H. Cha, M. Yoon, M. Park and J. Cho, *Adv. Energy Mater.*, 2018, **8**, 1702028.
5 W. Liu, P. Oh, X. Liu, M.-J. Lee, W. Cho, S. Chae, Y. Kim and J. Cho, *Angew. Chem., Int. Ed.*, 2015, **54**, 4440–4457.
6 H.-H. Ryu, B. Namkoong, J.-H. Kim, I. Belharouak, C. S. Yoon and Y.-K. Sun, *ACS Energy Lett.*, 2021, **6**, 2726–2734.
7 H. Gao, Q. Wu, Y. Hu, J. P. Zheng, K. Amine and Z. Chen, *J. Phys. Chem. Lett.*, 2018, **9**, 5100–5104.
8 J. Kim, J. Lee, H. Ma, H. Y. Jeong, H. Cha, H. Lee, Y. Yoo, M. Park and J. Cho, *Adv. Mater.*, 2018, **30**, 1704309.
9 C.-H. Jo, D.-H. Cho, H.-J. Noh, H. Yashiro, Y.-K. Sun and S. T. Myung, *Nano Res.*, 2014, **8**, 1464–1479.
10 J. Zhu, Y. Li, L. Xue, Y. Chen, T. Lei, S. Deng and G. Cao, *J. Alloys Compd.*, 2019, **773**, 112–120.
11 J. Yan, H. Huang, J. Tong, W. Li, X. Liu, H. Zhang, H. Huang and W. Zhou, *Interdiscip. Mater.*, 2022, **1**, 330–353.
12 S. S. Zhang and L. Ma, *J. Electrochem. Soc.*, 2021, **168**, 080512.
13 Y. Ding, B. Deng, H. Wang, X. Li, T. Chen, X. Yan, Q. Wan, M. Qu and G. Peng, *J. Alloys Compd.*, 2019, **774**, 451–460.
14 H. H. Sun, H.-H. Ryu, U.-H. Kim, J. A. Weeks, A. Heller, Y.-K. Sun and C. B. Mullins, *ACS Energy Lett.*, 2020, **5**, 1136–1146.
15 Z. Cui, X. Li, X. Bai, X. Ren and X. Ou, *Energy Storage Mater.*, 2023, **57**, 14–43.
16 T. He, L. Chen, Y. Su, Y. Lu, L. Bao, G. Chen, Q. Zhang, S. Chen and F. Wu, *J. Power Sources*, 2019, **441**, 227195.
17 J. Wang, C. Liu, G. Xu, C. Miao, M. Wen, M. Xu, C. Wang and W. Xiao, *Chem. Eng. J.*, 2022, **438**, 135537.
18 R. He, A. Wei, L. Zhang, W. Li, X. Bai and Z. Liu, *Solid State Ionics*, 2019, **337**, 56–62.
19 Z. Cui, Q. Xie and A. Manthiram, *ACS Appl. Mater. Interfaces*, 2021, **13**, 15324–15332.
20 H. Li, P. Zhou, F. Liu, H. Li, F. Cheng and J. Chen, *Chem. Sci.*, 2019, **10**, 1374–1379.
21 Y. Kim, H. Park, J. H. Warner and A. Manthiram, *ACS Energy Lett.*, 2021, **6**, 941–948.
22 Y. Kim, H. Park, K. Shin, G. Henkelman, J. H. Warner and A. Manthiram, *Adv. Energy Mater.*, 2021, 2101112.
23 T. Weigel, F. Schipper, E. M. Erickson, F. A. Susai, B. Markovsky and D. Aurbach, *ACS Energy Lett.*, 2019, **4**, 508–516.
24 Y. Su, L. Li, L. Chen, L. Wang, Y. Lu, Q. Zhang, L. Bao and F. Wu, *ACS Appl. Energy Mater.*, 2022, **5**, 2231–2241.
25 Q. Xie, W. Li, A. Dolocan and A. Manthiram, *Chem. Mater.*, 2019, **31**, 8886–8897.
26 Z. Luo, G. Hu, W. Wang, K. Du, Z. Peng, J. Zeng, L. Li and Y. Cao, *J. Power Sources*, 2022, **548**, 232092.
27 W. Yang, W. Xiang, Y.-X. Chen, Z.-G. Wu, W.-B. Hua, L. Qiu, F.-R. He, J. Zhang, B.-H. Zhong and X.-D. Guo, *ACS Appl. Mater. Interfaces*, 2020, **12**, 10240–10251.
28 S. F. Amalraj, R. Raman, A. Chakraborty, N. Leifer, R. Nanda, S. Kunnikuruvan, T. Kravchuk, J. Grinblat, V. Ezersky, R. Sun, F. L. Deepak, C. Erk, X. Wu, S. Maiti, H. Sclar, G. Goobes, D. T. Major, M. Talianker, B. Markovsky and D. Aurbach, *Energy Storage Mater.*, 2021, **42**, 594–607.
29 C. Roitzheim, L.-Y. Kuo, Y. J. Sohn, M. Finsterbusch, S. Möller, D. Sebold, H. Valencia, M. Meledina, J. Mayer, U. Breuer, P. Kaghazchi, O. Guillon and D. Fattakhova-Rohlfing, *ACS Appl. Energy Mater.*, 2021, **5**, 524–538.
30 K.-J. Park, H.-G. Jung, L.-Y. Kuo, P. Kaghazchi, C. S. Yoon and Y.-K. Sun, *Adv. Energy Mater.*, 2018, **8**, 1801202.
31 F. Li, Z. Liu, C. Liao, X. Xu, M. Zhu and J. Liu, *ACS Energy Lett.*, 2023, **8**, 4903–4914.
32 S. M. George, *Chem. Rev.*, 2010, **110**, 111–131.
33 Z. Li, J. Li, X. Liu and R. Chen, *Chem. Eng. Process.*, 2021, **159**, 108234.
34 X. Liu, Y. Su and R. Chen, *Int. J. Extreme Manuf.*, 2023, **5**, 022005.
35 J. Li, J. Xiang, G. Yi, Y. Tang, H. Shao, X. Liu, B. Shan and R. Chen, *Coatings*, 2022, **12**, 84.
36 C. Zhou, C. Dong, W. Wang, Y. Tian, C. Shen, K. Yan, L. Mai and X. Xu, *Interdiscip. Mater.*, 2024, **3**, 306–315.
37 F. Mattelaer, M. Van Daele, M. M. Minjauw, M. Nisula, S. D. Elliott, T. Sajavaara, J. Dendooven and C. Detavernier, *Chem. Mater.*, 2020, **32**, 4152–4165.
38 L. Chen, J. G. Connell, A. Nie, Z. Huang, K. R. Zavadil, K. C. Klavetter, Y. Yuan, S. Sharifi-Asl, R. Shahbazian-Yassar, J. A. Libera, A. U. Mane and J. W. Elam, *J. Mater. Chem. A*, 2017, **5**, 12297–12309.
39 Q. Li, W. Zhuang, Z. Li, S. Wu, N. Li, M. Gao, W. Li, J. Wang and S. Lu, *ChemElectroChem*, 2020, **7**, 998–1006.
40 J. Shen, B. Zhang, X. He, B. Xiao, Z. Xiao, X. Li and X. Ou, *J. Colloid Interface Sci.*, 2022, **629**, 388–398.
41 B. Oprea, T. Radu and S. Simon, *J. Non-Cryst. Solids*, 2013, **379**, 35–39.
42 A. Pilli, J. Jones, V. Lee, N. Chugh, J. Kelber, F. Pasquale and A. LaVoie, *J. Vac. Sci. Technol., A*, 2018, **36**, 061503.
43 A. Pilli, V. Lee, J. Jones, N. Chugh, J. Du, F. Pasquale, A. LaVoie and J. Kelber, *J. Phys. Chem. C*, 2020, **124**, 25846–25858.

44 X. Zeng, T. Jian, Y. Lu, L. Yang, W. Ma, Y. Yang, J. Zhu, C. Huang, S. Dai and X. Xi, *ACS Sustainable Chem. Eng.*, 2020, **8**, 6293–6304.
45 D. A. Hensley and S. H. Garofalini, *Appl. Surf. Sci.*, 1994, **81**, 331–339.
46 K. Nagao, M. Suyama, A. Kato, C. Hotehama, M. Deguchi, A. Sakuda, A. Hayashi and M. Tatsumisago, *ACS Appl. Energy Mater.*, 2019, **2**, 3042–3048.
47 Y. Liu, X. Wang, J. Cai, X. Han, D. Geng, J. Li and X. Meng, *J. Mater. Sci. Technol.*, 2020, **54**, 77–86.
48 N. Schulz, R. Hausbrand, C. Wittich, L. Dimesso and W. Jaegermann, *J. Electrochem. Soc.*, 2018, **165**, A833–A846.
49 L. Pan, Y. Xia, B. Qiu, H. Zhao, H. Guo, K. Jia, Q. Gu and Z. Liu, *J. Power Sources*, 2016, **327**, 273–280.
50 Y. Liu, X. Fan, B. Luo, Z. Zhao, J. Shen, Z. Liu, Z. Xiao, B. Zhang, J. Zhang, L. Ming and X. Ou, *J. Colloid Interface Sci.*, 2021, **604**, 776–784.
51 Y. Kim, D. Kim and S. Kang, *Chem. Mater.*, 2011, **23**, 5388–5397.
52 X. Li, J. Liu, M. N. Banis, A. Lushington, R. Li, M. Cai and X. Sun, *Energy Environ. Sci.*, 2014, **7**, 768–778.
53 H.-H. Sun and A. Manthiram, *Chem. Mater.*, 2017, **29**, 8486.
54 W. Bao, G. Qian, L. Zhao, Y. Yu, L. Su, X. Cai, H. Zhao, Y. Zuo, Y. Zhang, H. Li, Z. Peng, L. Li and J. Xie, *Nano Lett.*, 2020, **20**, 8832–8840.